Reactivity of the Binuclear Non-Heme Iron Active Site of Δ^9 Desaturase Studied by Large-Scale Multireference Ab Initio Calculations

Jakub Chalupský,[†,⊥] Tibor András Rokob,[†,∥] Yuki Kurashige,[⊥] Takeshi Yanai,[⊥] Edward I. Solomon,*[,‡] Lubomír Rulíšek,*[,†] and Martin Srnec*[,†,§]

[†]Institute of Organic Chemistry and Biochemistry, Academy of Sciences of the Czech Republic, Flemingovo náměstí 2, 166 10 Praha 6, Czech Republic

[§]J. Heyrovský Institute of Physical Chemistry, Academy of Sciences of the Czech Republic, Dolejškova 3, 182 23 Praha 8, Czech Republic

[‡]Department of Chemistry, Stanford University, 333 Campus Drive, Stanford, California 94305-5080, United States

[∥]Institute of Organic Chemistry, Research Centre for Natural Sciences, Hungarian Academy of Sciences, P.O. Box 286, H-1519 Budapest, Hungary

[⊥]Institute for Molecular Science, 38 Nishigo-Naka, Okazaki, Aichi 444-8585, Japan

S *Supporting Information*

ABSTRACT: The results of density matrix renormalization group complete active space self-consistent field (DMRG-CASSCF) and second-order perturbation theory (DMRG-CASPT2) calculations are presented on various structural alternatives for the O—O and first C—H activating step of the catalytic cycle of the binuclear nonheme iron enzyme Δ^9 desaturase. This enzyme is capable of inserting a double bond into an alkyl chain by double hydrogen (H) atom abstraction using molecular O_2. The reaction step studied here is presumably associated with the highest activation barrier along the full pathway; therefore, its quantitative assessment is of key importance to the understanding of the catalysis. The DMRG approach allows unprecedentedly large active spaces for the explicit correlation of electrons in the large part of the chemically important valence space, which is apparently *conditio sine qua non* for obtaining well-converged reaction energetics. The derived reaction mechanism involves protonation of the previously characterized 1,2-μ peroxy $Fe^{III}Fe^{III}$ (**P**) intermediate to a 1,1-μ hydroperoxy species, which abstracts an H atom from the C_{10} site of the substrate. An Fe^{IV}-oxo unit is generated concomitantly, supposedly capable of the second H atom abstraction from C_9. In addition, several popular DFT functionals were compared to the computed DMRG-CASPT2 data. Notably, many of these show a preference for heterolytic C—H cleavage, erroneously predicting substrate hydroxylation. This study shows that, despite its limitations, DMRG-CASPT2 is a significant methodological advancement toward the accurate computational treatment of complex bioinorganic systems, such as those with the highly open-shell diiron active sites.
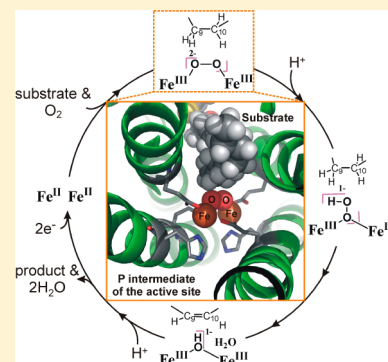
1. INTRODUCTION

Mono and binuclear nonheme iron (NHFe and $NHFe_2$) sites in proteins serve as efficient catalysts of many fundamental biological processes, such as DNA repair, neurotransmitter, antibiotic, natural product, and lipid biosynthesis, hypoxia response, and bioremediation.[1−6] The key step in their catalytic function is the activation of dioxygen by the iron site for its subsequent chemistry that includes hydroxylation and halogenation of unreactive aliphatic C—H bonds, electrophilic aromatic substitution, desaturation, epoxidation, and ring closure.[7]

The most prominent examples of $NHFe_2$ enzymes include soluble methane monooxygenase (sMMO) catalyzing conversion of methane to methanol,[8] ribonucleotide reductase (RNR) generating a tyrosyl radical necessary for reduction of nucleotides to deoxynucleotides,[9] toluene/o-xylene monoox-

ygenase (ToMO) and toluene 4-monooxygenase hydroxylase (T4MO) hydroxylating aromatic rings in toluene or o-xylene,[10,11] and Δ^9 desaturase (Δ^9D) performing insertion of one *cis* double bond into the alkyl chain of stearic acid to form oleic acid.[12,13] For several of these $NHFe_2$ systems, peroxodiferric intermediates (**P**) have been characterized experimentally (for the complete list, see ref 5 and refs 20−35 therein) or computationally.[14−16] In ToMO, evidence points to the direct involvement of such an intermediate in the reaction with the substrate,[17] whereas in MMO and RNR, **P** is thought to be converted to the high-valent $[Fe^{IV}_2(O)_2]$ diamond core **Q**[18] and the mixed valent (Fe^{III}—O—Fe^{IV})
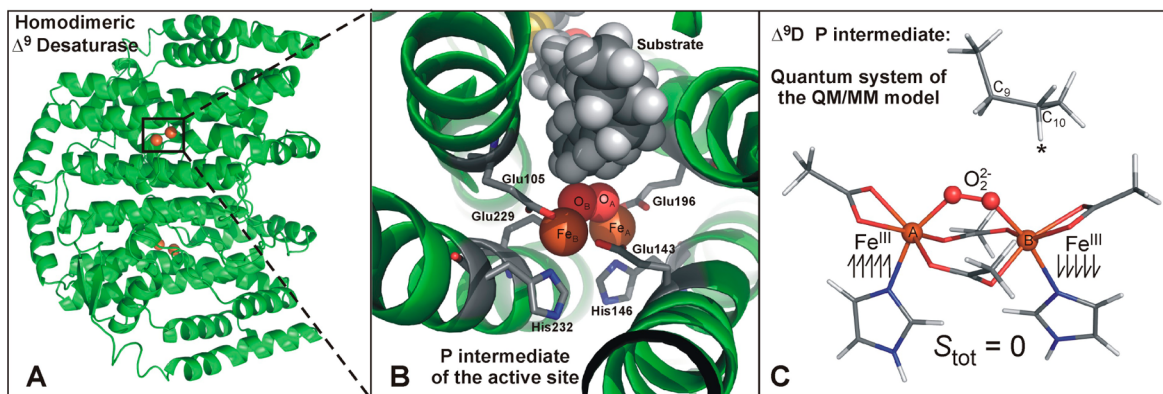
Figure 1. (A) Homodimer of Δ^9 desaturase with two NHFe$_2$ active sites (orange spheres represent Fe atoms). (B) One of the two active sites in the **P** intermediate (with 1,2-μ binding mode for O$_2$) in the presence of the substrate. The ligating residues are displayed as sticks. The structure is taken from the QM/MM model from ref 16. (C) The quantum region of the QM/MM model of the Δ^9D **P** intermediate. The star indicates an aliphatic H atom that has to be abstracted as the first step of the insertion of the double bond between the C$_{10}$ and C$_9$ sites during the catalysis.

X[19,20] species, respectively, which are responsible for the oxidation chemistry. These structures have also been the subjects of detailed calculations.[21−24] Importantly, it appears that the reaction mechanisms of these enzymes with apparently similar active sites are fine-tuned for their specific chemistry. Moreover, Δ^9D is capable of performing both the dehydrogenation (desaturation) chemistry with its native substrate or hydroxylation/scission with modified substrates.[12,25−27] The same dual reactivity (desaturation vs hydroxylation) has been observed for the NHFe$_2$ alkane ω-hydroxylase, AlkB.[28] Therefore, it is highly desirable to have quantitatively accurate theoretical methods complementing the significant amount of spectroscopic, kinetic, and thermodynamic experimental data since a number of pertinent questions, in particular, the preference for a given catalytic pathway, can be directly addressed by means of computational chemistry.

Iron, in any of its common formal oxidation states, is a highly open-shell system, and its complexes belong to the most difficult systems to be studied by quantum chemistry. They typically demand a multireference treatment for the correct description of the wave function, and almost quantitative accuracy has indeed been achieved in certain cases using the complete or restricted active space self-consistent field methods (CASSCF/RASSCF) combined with second-order perturbation theory (CASPT2/RASPT2). These methods provided notable results for heme and some mononuclear nonheme intermediates[29−32] and also for other polynuclear metal sites in proteins, such as spin-frustrated trinuclear copper sites in multicopper oxidases.[33−35] Nevertheless, for the evaluation of the relative energies of intermediates and transition states in NHFe or NHFe$_2$ catalytic sites in general, the active space often requires a number of active orbitals and active electrons that far exceeds the computationally affordable limit of the conventional CASSCF/CASPT2 method due to the exponential scaling of the costs with active space size. Hence, to date, there does not exist a general and robust computational strategy that would treat all of the iron complexes with sufficient accuracy,[36] and many other NHFe and NHFe$_2$ reactive intermediates have thus been elusive to quantitative computational treatment using *ab initio* methods. This severe computational limitation suggests that density functional theory (DFT) methods can be considered as the only practical solution for the description of these electronically intricate systems. However, various functionals give quite different results for the kinetics,

thermodynamics, and spectroscopic parameters, and we are not aware of a benchmark study critically evaluating their performance for NHFe$_2$ systems. One of the reasons is definitely the absence of a reliable and affordable reference method, represented by the "gold standard" coupled cluster, CCSD(T), in the realm of small closed-shell systems and their intermolecular interactions,[37] which would provide guidance for the development and usage of cheaper approaches.

An emerging alternative for these intrinsically complex electronic systems encountered in bioinorganic chemistry is the density matrix renormalization group (DMRG) approach,[38] which represents a recent breakthrough in the technology of multireference calculations. Since its original invention for solving strong-correlation problems in condensed matter physics, it has been shown that the special parametrization built into the DMRG wave function makes it very useful also for the application to *ab initio* quantum chemistry.[39−42] It offers a compressed, compact representation of nonperturbative electron correlation and associated quantum entanglement. It is now clear that DMRG is best applied within the complete-active space (CAS) formalism and used as a direct replacement for the CAS configuration interaction (CAS-CI) method to describe static correlation.[41,43] Combined with this scheme, the dynamic correlation can also be included using the weak correlation treatments based on CASPT2 theory or canonical transformation (CT) theory.[44] The combination of the active-space DMRG reference with CASPT2 and CT is called DMRG-CASPT2[45] and DMRG-CT,[46] respectively.

The strength of DMRG is that it allows the use of a large-size active space in multireference calculations, overcoming the exponential scaling of conventional CASSCF with respect to the size of the active space, which makes the conventional calculations prohibitively expensive for an active space larger than approximately 15 electrons in 15 orbitals (15e,15o). Quasi-one-dimensional π conjugated systems are a domain of applications for which the DMRG is most powerful, permitting CAS(100e,100o) or larger, but remarkably large active spaces can be employed also in the case of (bio)inorganic systems, which has been exploited only recently. The relative energy difference of [Cu$_2$O$_2$]$^{2+}$ isomers, recognized as a challenging bioinorganic prototype,[47] was first calculated by Reiher and co-workers using the DMRG method[48,49] and later re-examined by Kurashige and Yanai with a better-conditioned DMRG at a near-exact full CI level in a large CI space (32e,62o), partially

Scheme 1. Proton- and Water-Assisted Possible Mechanisms of O$_2$ Activation in Δ^9D, from ref 16[a]
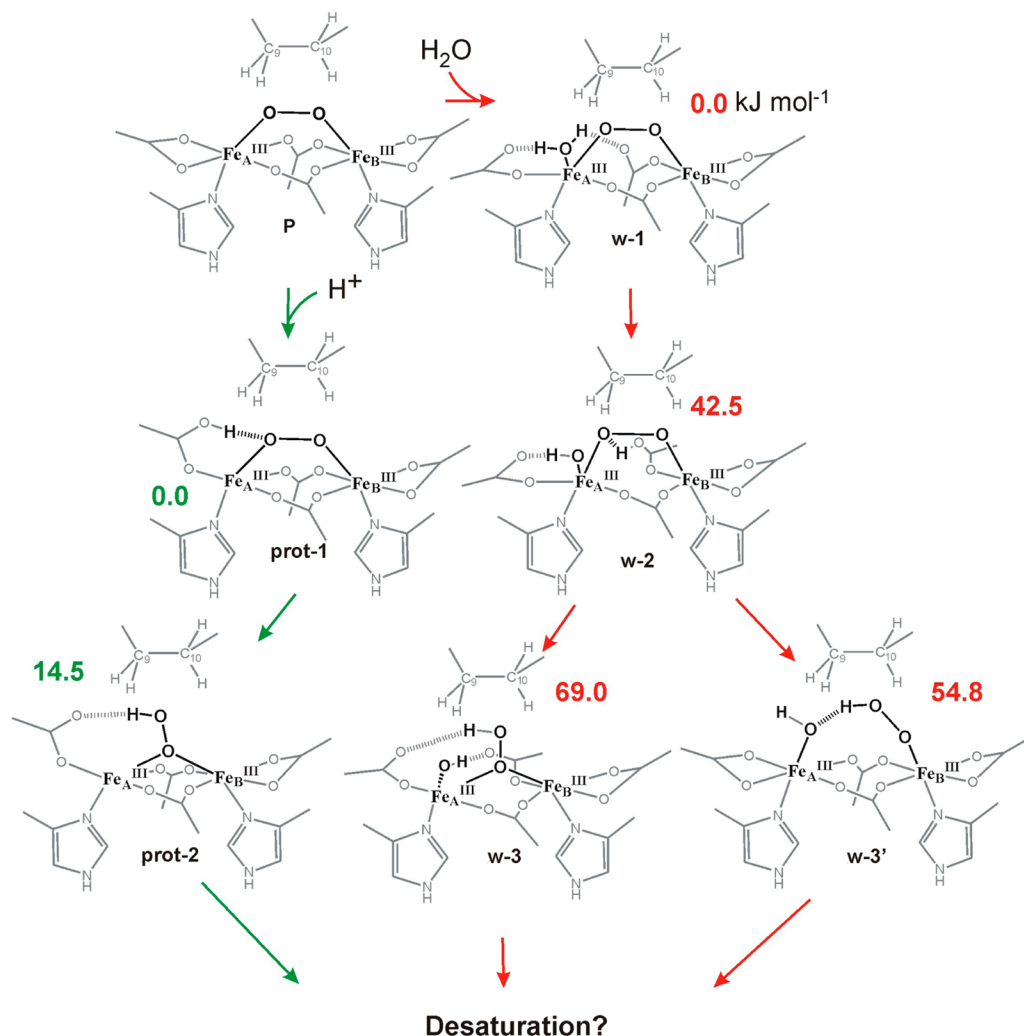
[a] The depicted relative energies are calculated at the QM(B3LYP/def2-TZVP//RI-BP86/def2-SVP)/MM level. Note that the **P**, **prot-1**, **w-1**, and **w-2** species are not reactive towards C$_{10}$–H bond cleavage according to QM(DFT)/MM scans (see Figure S1).

treating dynamic correlation effects.[50] Similar results were also obtained by using quantum information theory (QIT) within the DMRG formalism,[51] which finally reconciled the problems of varying active spaces for solving the [Cu$_2$O$_2$]$^{2+}$ system. However, the most prominent recent application of DMRG in bioinorganic chemistry is the theoretical investigation of the entangled quantum electronic wave functions of the Mn$_4$CaO$_5$ cluster in photosystem II.[52] These applications highlight the benefits from the use of a large active space, namely: (i) the increased flexibility in selecting active orbitals and the possibility of including the large number of important orbitals necessary to describe a reacting polynuclear transition-metal system; (ii) the possibility of managing the well-known numerical difficulties in the convergence of CASSCF orbital optimization by enlarging the active space in a way that suppresses the orbital switching. The binuclear iron systems including Δ^9D studied here are excellent multireference targets, for which we can take advantage of these abilities of DMRG methods.

Stearoyl-acyl carrier protein Δ^9 desaturase (Δ^9D) is a homodimeric enzyme with an NHFe$_2$ core in each monomer unit (Figure 1A), which catalyzes the dehydrogenation of a

CH$_2$–CH$_2$ moiety of the alkyl chain of stearic acid with the concomitant reduction of dioxygen to water:

$$-CH_2-CH_2- + O_2 + 2e^- + 2H^+$$
$$\rightarrow -CH=CH- + 2H_2O$$
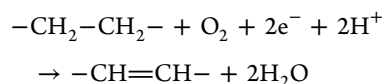
The two exogenous electrons originate from NADPH and are transferred through a ferredoxin/ferredoxin reductase chain to the diiron core, along with two exogenous protons from the solvent. The removal of the H atoms occurs regiospecifically and in a stepwise manner, the first coming from C$_{10}$ and the second from C$_9$. The resting state of the enzyme is diferric, which upon reduction by the two electrons provided by ferredoxin is converted to the diferrous form. This form is capable of O$_2$ activation, followed by abstraction of two H atoms from the substrate and formation of the water molecule together with the simultaneous reoxidation of the enzyme into the diferric resting state.

If dithionite is used as reducing agent in the *in vitro* preparation of the diferrous Δ^9D enzyme instead of the *in vivo* partner ferredoxin, the addition of oxygen leads to an isolable peroxodiferric intermediate (**P**), which has been characterized spectroscopically. It has been shown that this **P** intermediate
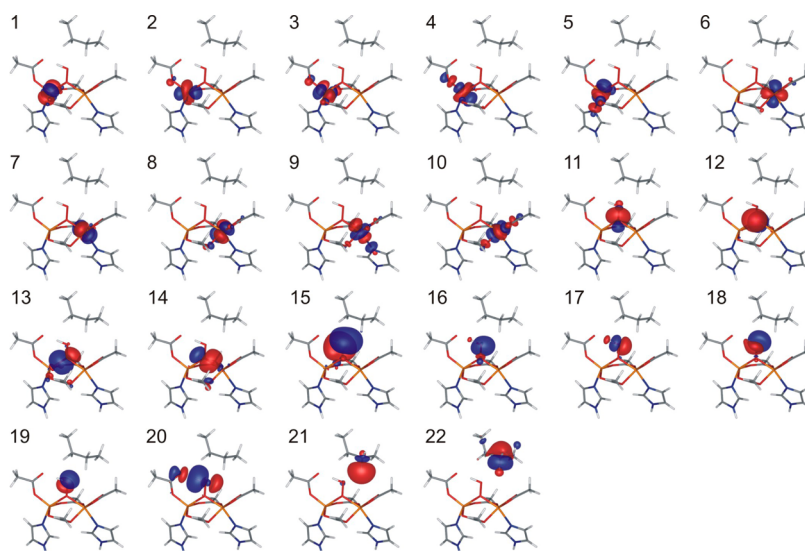
Figure 2. Localized DMRG-CASSCF active orbitals for a 1,1-μ hydroperoxodiferric complex (reactant structure of pathway **2** - Scheme 2, *vide infra*), and their ordering in the active space. Orbitals are ordered according to their localization to particular atoms of the series Fe_A, Fe_B, O, O, H (O—O—H), H (C_{10}—H), and C_{10}.

has the $S = 0$ ground state arising from two antiferromagnetically coupled high-spin ($S_{Fe} = 5/2$) Fe^{III} centers, which are bridged by two Glu residues and peroxide ligand. In our previous study[16] dealing with the computational and spectroscopic definition of key intermediates in the initial steps of the Δ^9D catalytic cycle, we identified this species to have a 1,2-μ-peroxo structure (Figure 1B,C).

Nevertheless, this intermediate is not capable of H atom abstraction from the substrate. Two possible reasons have been proposed to explain the absence of reactivity: (i) the **P** intermediate might not be the catalytically relevant intermediate *in vivo*; (ii) **P** might be part of the "catalytic cycle" but must be converted into another (activated) intermediate prior to H atom abstraction. The biochemical relevance of **P** is supported by the observation that in structurally related enzymes (RNR,[9,15] MMO,[8] ToMO[10]) a 1,2-μ peroxodiferric (**P**) intermediate was found to be associated with the *in vivo* chemisry. Moreover, mutagenesis studies on RNR and ToMO revealed the existence of another peroxodiferric (**P′**) intermediate, which may be short-lived in the wild-type enzymes and correlates with the native reactivity.[53,54] An analogous activated **P′** intermediate can be envisioned also for Δ^9D, although no such species has yet been observed.

In Δ^9D, two plausible activation pathways (**P** → **P′**) were proposed on the basis of computations,[16] where either a proton or a water perturbs the **P** active site (Scheme 1). Although the suggested **P′** intermediates in Δ^9D are energetically accessible, no further reaction step along the reaction coordinate of H atom abstraction was investigated in detail, mostly due to the inability of DFT methods to describe the electronic structure of the reaction intermediates with a sufficient degree of accuracy.

We pursue two main goals in the present study. The first is a thorough investigation of the H atom abstraction and the associated O—O cleavage as key steps in the Δ^9D reaction mechanism, starting from various candidates for **P**/**P′** structures. In addition to the previously suggested[16] proton- and water-perturbed **P′**s, we also examine the addition of an electron or of an electron/proton couple to the **P** intermediate as other possible activation factors. While this may not be relevant to Δ^9D,[55] it might be so for the conversion of **P** to the

mixed-valent **X** species in RNR. To study these systems with highly multireference character, we employ the DMRG-CASPT2 method to select the most viable structural candidates and energetically characterize the reaction steps. Our second goal is to compare the performance of eight popular DFT functionals (see Section 2.2) against these highly correlated multireference DMRG-CASPT2 calculations in order to identify an appropriate functional for the exploration of both the full Δ^9D catalytic cycle and the reactivity of $NHFe_2$ species in general. To the best of our knowledge, this is the first application of the DMRG-CASPT2 (i.e., inclusion of dynamical correlation into a large active-space multireference calculation) in enzymatic reactivity, and therefore, we consider the present study as a crucial methodological step in modeling the structure, energetics, and reactivity of the $NHFe_2$ enzymes.

2. COMPUTATIONAL DETAILS

2.1. Density Matrix Renormalization Group (DMRG) Calculations. The *ab initio* DMRG[38] complete active space self-consistent field (DMRG-CASSCF) and complete active space second-order perturbation theory (DMRG-CASPT2) calculations presented in this work were carried out using the ORZ quantum chemistry package, developed in the group of Prof. T. Yanai. For all atoms, the ANO-RCC basis set, contracted to [6s4p3d2f] for Fe, [3s2p] for O, N, and C, and [2s] for H, was used.[56] In all DMRG calculations, scalar relativistic effects were included via the second-order Douglas—Kroll—Hess (DKH2) one-electron spin-less Hamiltonian.[57]

The DMRG-CASSCF active spaces include all $3d_{Fe}$-based molecular orbitals, all O_2-originating valence orbitals, σ and σ^* orbitals of the substrate C—H bond, and all valence orbitals of the water molecule (if present, see Scheme 1). This results in an active-space size varying from $(26e,20o)$ to $(35e,26o)$. In order to improve the accuracy and convergence of DMRG calculations,[58] active orbitals were localized using the Pipek—Mezey scheme[59] and ordered according to their spatial localization. For a representative structure (a 1,1-μ hydroperoxo species; reactant of pathway 2, **R₂**, *vide infra*), active-space orbitals are depicted in Figure 2, which illustrates the localized orbital scheme and the ordering used for all reactants and most transition states: Fe_A (with the O—H group in water-assisted pathways), Fe_B, the (H)O—O moiety, and the C_{10}—H σ and σ^* orbitals. Analogously, for the rest of the transition states and all products, the fragments with localized

Scheme 2. Nine Conceived Reaction Pathways for the Key Step in the Δ⁹D Catalytic Cycle^a

	R → TS → P	Type of reaction (Activation factor)
(1)		C–H cleavage (—)
(2)		C–H cleavage (H⁺)
(3)		C–H cleavage (H₂O)
(4)		O–O cleavage (H⁺)
(5)		O–O cleavage (H⁺)
(6)		O–O cleavage (e⁻)
(7)		C–H cleavage (H⁺ e⁻)
(8)		O–O cleavage (H⁺ e⁻)
(9)		C–H cleavage (H₂O e⁻)

^{a}The structures for reactants (**R**, left), transition states (**TS**, middle), and products (**P**, right) are depicted schematically. DMRG and DFT energy profiles for these reaction pathways are given in Tables 1 and 2, respectively. Note that the reactant in reaction 1 is the 1,2-μ **P** intermediate, whereas reactants in **2** and **3** are **prot-2** and **w-3′** structures in Scheme 1, taken from ref 16.

orbitals are in the following order: Fe_A, $(H)O_{FeA}$, Fe_B, $(H)O_{FeB}/H_2O_{FeB}$ (and O−H), and H−C_{10} or C_{10}.

All DMRG-CASSCF orbital optimizations were performed with 256 spin-adapted renormalized many-electron basis functions ($M = 256$), which already yields, owing to the proper orbital ordering, satisfactory results. Final DMRG-CASSCF wave functions were obtained by solving the CASCI problem using $M = 512$. It can be mentioned that the maximum difference in absolute energies between $M = 256$ and 512 calculations was found to be 2.4 kJ mol^{-1} (10^{-3} au) for structure R_9 (26 orbitals in the active space), whereas most of other pairs (256 vs 512) differed by <0.1 kJ mol^{-1}, yielding the average difference of ~0.2 kJ mol^{-1} for both absolute and relative energies. Thus, all DMRG-CASSCF solutions used in this work can be considered well converged with respect to M for "chemical" purposes. In fact, the solution should be very close to the conventional full-CI CASSCF limit in many cases. All DMRG wave functions were spin-adapted,[60] and the total spin state of $S = 0$ (or $S = 1/2$) was calculated. This ground-state spin multiplicity is in agreement with available experimental data and independently confirmed by our test calculations for selected pathways based on conventional CASSCF/CASPT2 methodology (see Table S6 and discussion therein). The formal oxidation states of individual atoms and groups were determined by natural-orbital analysis.

Finally, we accounted for the effects of dynamic correlation by performing the noniterative DMRG-CASPT2 calculations, assuming a diagonal zero-order Hamiltonian. In all of these calculations, the 1s, 2s, and 2p orbitals of Fe atoms and 1s orbitals of first-row atoms were not correlated, and an imaginary level shift of $i0.3$ au and an IPEA level shift of 0.25 au were used.

2.2. Density Functional Theory Calculations. DFT calculations reported in this study were carried out using the Turbomole 6.3[61] and Gaussian09 programs.[62] The BP86,[63] M06-L,[64] TPSS,[65] τ-HCTH,[66] TPSSh,[67] B3LYP,[68] B3LYP-D3 (with zero-damping dispersion correction),[68,69] M06,[70] and ωB97X-D[71] functionals were used. The nonhybrid DFT (BP86 and TPSS) calculations were expedited by expanding the Coulomb integrals in an auxiliary basis set, the resolution-of-identity (RI-J) approximation.[72,73] Unless otherwise mentioned, the active-site structures studied in this work were optimized at the QM(RI-BP86/def2-SVP)/MM level using the ComQum program[74] and the same computational protocol as in ref 16. The basis set convergence with respect to the accuracy of equilibrium geometries was further verified by carrying out several geometry optimizations for reaction 2 (*vide infra*), using the larger def2-TZVP basis set. Only negligible geometric changes were observed in comparison with the def2-SVP equilibrium geometries. The single point energies were recomputed using def2-TZVP. The structural models for the active site, corresponding to the quantum regions in the QM/MM calculations, consisted of 60−70 atoms and included two iron ions, four acetates, two imizadoles, one butane, and possibly one water molecule or one proton (Figure 1C).

2.3. Hybrid QM/MM Calculations. In the QM/MM scheme employed, the protein structure is partitioned into three regions: (i) System 1, which represents the enzymatic active site and is treated by quantum mechanics; (ii) Systems 2 and 3, which are described by molecular mechanics where atoms in System 2 are allowed to move and atoms in System 3 are kept fixed during QM(DFT)/MM optimizations. A hydrogen link atom scheme is employed, and the electrostatic interaction between System 1 and Systems 2 and 3 is described at the QM level by including the latter atoms as point charges in the DFT calculations. For more details, see ref 16.

Total reaction (activation) QM(DMRG)/MM energies are calculated as

$$\Delta E_{DMRG/MM}^{(\ddagger)} = \Delta E_{DMRG\text{-}vac}^{(\ddagger)} + \Delta E_{ptchgs}^{(\ddagger)} + \Delta E_{MM23}^{(\ddagger)} \quad (1)$$

where $\Delta E_{DMRG\text{-}vac}^{(\ddagger)}$ is the *in vacuo* DMRG-CASPT2 energy difference in System 1, $\Delta E_{ptchgs}^{(\ddagger)}$ is the energy change along a reaction coordinate arising from the contribution of electrostatic interaction of System 1 with Systems 2 and 3, calculated at the DFT level as $\Delta E_{ptchgs}^{(\ddagger)} = \Delta E_{DFT\text{-}ptchgs} - \Delta E_{DFT\text{-}vac}$, and $\Delta E_{MM23}^{(\ddagger)}$ describes the MM energy

change (including electrostatics) within Systems 2 and 3 as well as the change in the MM coupling terms between System 1 and Systems 2 and 3. This small detour from the standard QM/MM energy expression must be taken because point charges are not currently implemented in the one-electron part of the DMRG Hamiltonian used in ORZ. In the MM calculations of the QM/MM forces and energies, all atoms are represented by the Cornell force field.[75]

The reaction (activation) Gibbs free energy ($\Delta G^{(\ddagger)}$) was estimated according to the relation:

$$\Delta G^{(\ddagger)} = \Delta E_{DMRG/MM}^{(\ddagger)} + \Delta E_{ZPE}^{(\ddagger)} - RT\Delta(\ln q_{trans}q_{rot}q_{vib})^{(\ddagger)} \quad (2)$$

where $\Delta E_{ZPE}^{(\ddagger)}$ is the change in the zero-point vibrational energy of isolated System 1 optimized without any geometric constraints in the gas phase, and $RT\Delta(\ln q_{trans}q_{rot}q_{vib})^{(\ddagger)}$ accounts for the change in entropic terms and in the thermal correction to the enthalpy, obtained from the harmonic vibrational frequencies via the ideal-gas, rigid-rotor, harmonic-oscillator approximation at $T = 298.15$ K. All thermodynamic corrections were obtained at the DFT(BP86) level of theory. Note that these ZPE and other entropic/thermal corrections are considered as crude approximations to the corresponding terms in QM/MM free energies.

3. RESULTS AND DISCUSSION

3.1. Description of the O−O and C−H Activation Steps in the Δ^9D Catalytic Cycle. On the basis of earlier DFT computations as well as literature results, we conceived nine possible candidate reactions to evaluate in this study that might represent the key step of the Δ^9D catalytic cycle. These pathways are depicted in Scheme 2 and correspond either to the cleavage of the peroxo O−O bond or to the cleavage of both the C−H and O−O bonds in a single step. As the starting point, we consider the direct abstraction of the C_{10}−H hydrogen atom by the "unactivated" **P** intermediate having the 1,2-μ peroxo structure (Scheme 2, path **1**). Eight alternative reaction pathways are evaluated (paths **2−9**), which involve a reactant that is derived from **P** via activation by a proton (**2, 4, 5**), water molecule (**3**), electron (**6**), electron/proton couple (**7** and **8**), or electron and water molecule (**9**). These pathways are discussed below.

3.1.1. Activation of the Peroxy-Level Intermediate by a Proton (Scheme 2: pathways 2, 4, 5). The rationale behind selection of these pathways as plausible candidates for the initial steps in Δ^9D reaction mechanism is provided by experimental and theoretical studies on related enzymes. The activation of **P** in RNR,[15,76] MMO,[10] and ToMO/T4MO[14] was suggested to proceed through protonation of the active site. While in both RNR and MMO, protonation activates the diferric site via O−O(H) cleavage to yield either the reasonably well-characterized μ-oxo $Fe^{III}Fe^{IV}$ **X** intermediate in RNR (protonation coupled with one-electron reduction) or the $Fe^{IV}Fe^{IV}$ **Q** intermediate in MMO (only protonation), no O−O cleavage seems to be involved prior to arene oxidation in ToMO/T4MO. The situation seems to be similar in Δ^9D, for which it was suggested[16] that the protonation of the active site leads to a 1,1-μ hydroperoxo $Fe^{III}Fe^{III}$ species, an intermediate which could then be responsible for the substrate C_{10}−H bond cleavage (path **2** in Scheme 2).

In contrast to RNR and MMO, the QM(B3LYP)/MM and QM(M06)/MM calculations[16] indicated that the direct cleavage of the O−O bond of the 1,2-μ peroxo moiety in carboxy-protonated Δ^9D **P**, which would result in an $Fe^{IV}Fe^{IV}$ complex, is not energetically feasible (barrier of ~150 kJ mol^{-1}). However, since two other DFT functionals employed in the QM/MM scheme (BP86 and TPSS) predicted much

Table 1. Activation and Reaction Energies (in kJ mol⁻¹) Calculated by the DMRG Method for the Investigated Reaction Pathways (depicted in Scheme 2)ᵃ

	reaction and structure	ΔE (CASSCF) kJ mol⁻¹	ΔE (CASPT2) kJ mol⁻¹	electronic structure
1ᵇ	R_1	0.0 [CAS(26e,20o)]	0.0	[Fe^{III}(O−O)$^{2-}$Fe^{III} H−C]
	TS_1 "concerted"ᶜ	226.1	89.8	[Fe^{IV}=O^{2-} Fe^{IV}=O^{2-}···H···C]/[Fe^{IV}=O^{2-} Fe^{III}−O$^{\bullet-}$···H···C]
	TS_1 "stepwise"ᶜ	144.2	102.6	[Fe^{III}(O···O)$^{2-}$ Fe^{III} H−C]/[Fe^{IV}=O^{2-} Fe^{IV}=O^{2-} H−C]
	P_1	70.4	−3.9	[Fe^{IV}=O^{2-} Fe^{III}(OH)$^{1-}$ C$^\bullet$]
2	R_2	0.0 [CAS(26e,22o)]	0.0	[Fe^{III} Fe^{III} (O−OH)$^{1-}$ H−C]
	TS_2	86.6	54.9	[Fe^{III} Fe^{III}{O$^{\bullet-}$···OH···H···C}]
	P_2	35.1	3.4	[Fe^{IV}=O^{2-} Fe^{III}OH$_2$ C$^\bullet$]
	TS_2 "hydroxylated"	≫90ᵈ	−	[Fe^{III} Fe^{III}{O$^{\bullet-}$···OH···$^-$H···C$^{\bullet+}$}]
	P_2 "hydroxylated"	−273.8	−254.6	[Fe^{III} Fe^{III}(OH)$^{1-}$ HO−C]
3	R_3	0.0 [CAS(34e,26o)]	0.0	[Fe^{III}(OH)$^{1-}$ Fe^{III}(O−OH)$^{1-}$ H−C]
	TS_3	286.6	150.3	[Fe^{III}(OH)$^{1-}$ Fe^{III}{O$^{\bullet-}$···OH···H···C}]
	P_3	123.7	9.4	[Fe^{III}(OH)$^{1-}$ Fe^{IV}=O^{2-} H$_2$O C$^\bullet$]
4ᵇ	R_4	0.0 [CAS(26e,20o)]	0.0	[Fe^{III}(O−O)$^{2-}$Fe^{III} H−C]
	TS_4	126.0	118.1	[Fe^{III}(O···O)$^{2-}$ Fe^{III} H−C]/[Fe^{IV}=O^{2-} Fe^{IV}=O^{2-} H−C]
	P_4	109.5	14.3	[Fe^{IV}=O^{2-} Fe^{IV}=O^{2-} H−C]
5	R_5	0.0 [CAS(26e,21o)]	0.0	[Fe^{III}(HO−O)$^{1-}$Fe^{III} H−C]
	TS_5	103.9	41.9	[Fe^{III}(HO···O)$^{1-}$Fe^{III} H−C]
	P_5	285.9	154.7	[Fe^{IV}(OH)$^{1-}$ Fe^{IV}=O^{2-} H−C]
6	R_6	0.0 [CAS(27e,20o)]	0.0	[Fe^{II}(O−O)$^\bullet$$^-$Fe^{II} H−C]ᵉ
	TS_6	161.8	40.3	[Fe^{II}(O···O)$^\bullet$$^-$Fe^{II} H−C]/[Fe^{II}(O···O$^{\bullet-}$)Fe^{II} H−C]ᵉ
	P_6	139.6	0.4	[Fe^{IV}=O^{2-} Fe^{III}−O^{2-} H−C]
7	R_7	0.0 [CAS(27e,21o)]	0.0	[Fe^{III} Fe^{II}(O−OH)$^{1-}$ H−C]
	TS_7	31.4	64.9	[Fe^{III} Fe^{II}(O···OH)$^{1-}$ H−C]
	P_7	−25.5	−78.6	[Fe^{III}−O^{2-}Fe^{III} H$_2$O C$^\bullet$]
8	R_8	0.0 [CAS(27e,20o)]	0.0	[Fe^{II}(O−O)$^{2-}$Fe^{III} H−C]
	TS_8	−3.7	−6.0ᶠ	[Fe^{II}(O···O)$^{2-}$Fe^{III} H−C]
	P_8	−42.4	−63.9	[Fe^{II}(OH)$^{1-}$ Fe^{IV}=O^{2-} H−C]
9	R_9	0.0 [CAS(35e,26o)]	0.0	[Fe^{III}(OH)$^{1-}$ Fe^{II}(O−OH)$^{1-}$ H−C]
	TS_9	226.9	86.9	[Fe^{III}(OH)$^{1-}$ Fe^{II}{O$^{\bullet-}$···OH···H···C}]
	P_9	131.1	−67.7	[Fe^{III}−O^{2-} Fe^{III}(OH)$^{1-}$ H$_2$O C$^\bullet$]

ᵃThe S = 0 or 1/2 (the latter in the presence of an exogenous electron) total electronic spin states are considered throughout. The values represent *in vacuo* single-point energies of the QM regions obtained for the QM(BP86/def2-SVP)/MM equilibrium geometries. The steric, ΔE_{MM23}, and electrostatic, ΔE_{ptchgs}, QM/MM corrections to the *in vacuo* activation and reaction energies (see eq 1) are listed in Table S1. ᵇMaxima and minima of the DMRG-CASPT2 energy along the one-dimensional reaction path calculated at the QM(BP86/def2-SVP)/MM level. Note that the location of these extrema is shifted along the reaction coordinate with respect to those of the QM(BP86/def2-SVP)/MM PES (for an example, see Figure S5). ᶜTechnical details on how these TSs were calculated are explained in ref 79. ᵈSee more details on how the value was obtained in ref 84. ᵉThe electronic structures with a peroxide character [Fe^{II}−O$_2$$^{2-}$−Fe^{III}] are higher in energy (e.g., for TS$_6$, it is ∼30 kJ mol⁻¹ above the ground state). ᶠThe negative value for $\Delta E^\ddagger_{DMRG}$ calculated on top of the QM(BP86)/MM optimized structure indicates no barrier in this process. Nevertheless, this "transient" structure is labeled as TS$_8$.

lower reaction barrier of ∼40 kJ mol⁻¹,[16] this reaction step is re-evaluated here using the highly correlated multireference DMRG methods (path 4 in Scheme 2). For the sake of completeness, we also included the O−O cleavage in the peroxo-protonated isomer (path 5). Study of this six-coordinate, six-coordinate (abbreviated as 6C,6C) 1,2-μ hydroperoxo-Fe^{III}Fe^{III} species is also motivated by the fact that it is very close in energy to the reactant of path 2, i.e., to the (5C,6C) 1,1-μ hydroperoxo-Fe^{III}Fe^{III} complex.

3.1.2. Activation of the Peroxy-Level Intermediate by Water (pathway 3). A water adduct (w-1 in Scheme 1) was recently suggested to be one of two plausible candidates for

activated peroxy-level intermediates.[15,16] While this intermediate has been shown to have spectroscopic features similar to **P′** in RNR (ref 15), DFT calculations indicate that the energy profile of the subsequent step, i.e., the C$_{10}$−H or O−O bond cleavage, is very similar to the corresponding reaction of unactivated **P** (see Figure S1). This peroxy-level intermediate was therefore further converted through deprotonation of the Fe$_A$-bound water molecule (yielding w-2 in Scheme 1) and then via rearrangement into the w-3 and w-3′ intermediates, both containing a reactive HOO−Fe^{III} unit. Although w-3 and w-3′ lie ∼69 and 55 kJ mol⁻¹ higher in energy than w-1, respectively, the C$_{10}$−H bond activation by the high-spin (S =
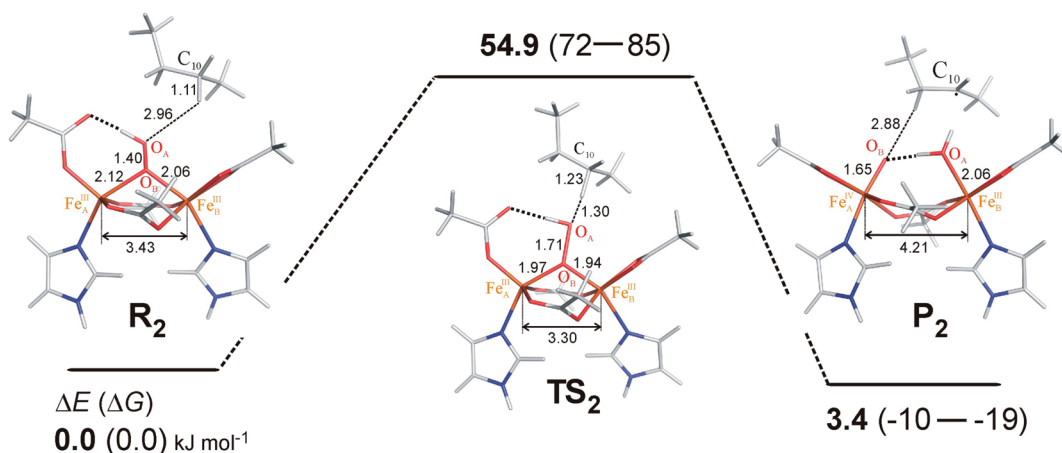
Figure 3. Active-site structures of reactant, transition state, and product of reaction pathway **2** (see Scheme 2) and their relative DMRG-CASPT2(26e,22o) energies for the singlet states (with ΔG estimates[81] in parentheses), in kJ mol^{-1}. All distances are in Å.
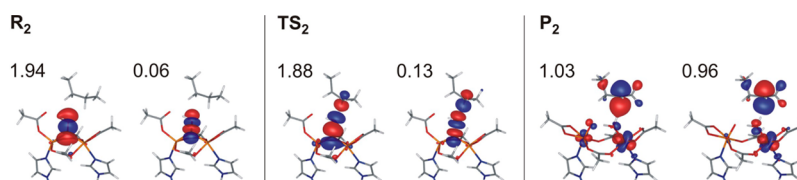

Figure 4. Evolution of the most important DMRG-CASSCF(26e,22o) active natural orbitals and their occupation numbers in going from **R$_2$** through **TS$_2$** to **P$_2$** (structures displayed in Figure 3), clearly demonstrating homolytic cleavage of C$_{10}$–H. The singly occupied C$^\bullet$ p orbital of **P$_2$** appears in combination with a d orbital of Fe$_B$.

5/2) HOO–Fe$_B^{III}$ unit in **w-3′** was included among the pathways investigated (path **3** in Scheme 2).

3.1.3. Activation of the Peroxy-Level Intermediate by an Electron (pathways 6–9). Δ^9D is a homodimeric enzyme, which raises the possibility of some interaction between the diiron centers of the two subunits that may be relevant for the catalytic cycle or for other observed reactivity. As hypothesized in ref 77, the decay of the *in vitro* prepared **P** intermediate into the Fe^{III}–O–Fe^{III} product without desaturation of the substrate may be triggered by two electrons provided by the other, 23 Å-distant diiron center in the Fe^{II}Fe^{II} oxidation state. In the present study, we further consider the possibility of one-electron reduction of the *in vivo* formed Δ^9D **P** (or another peroxy-level) intermediate by the second active site (in a state different from **P**) through an intersubunit electron transfer (IET) pathway (for more details, see Figure S2 and related discussion in Supporting Information (SI)). This suggestion would be also in line with the activation of the peroxy-level intermediate in the RNR enzyme, where 1,2-μ **P** is converted through proton-coupled electron transfer (PCET) to the **X** intermediate, which performs H atom abstraction from the hydroxyl group of Tyr122.[78] From this point of view, reaction steps (paths **6–9** in Scheme 2) initiated by 1e$^-$ reduction of selected peroxy-level intermediates are of interest: (i) Reductive cleavage of the O–O bond would allow for an [Fe^{III}–O$^-$–Fe^{IV}=O] intermediate potentially reactive toward H atom abstraction (reaction **6** in Scheme 2); (ii) 1e$^-$ reduction would modify the energetics of the homolytic C$_{10}$–H and O–O bond cleavages in protonated forms, derived from **prot-1** and **prot-2** in Scheme 1 (reactions **7** and **8** in Scheme 2), with the latter being potentially relevant to RNR chemistry; and (iii) also, 1e$^-$ reduction would tune the energetics of the homolytic C$_{10}$–H

bond cleavage in water-assisted form (derived from **w-3′** in Scheme 1; reaction **9** in Scheme 2).

3.2. DMRG-CASPT2 Calculations for All Pathways. The results of DMRG-CASSCF and DMRG-CASPT2 calculations for the activation barriers and reaction energies of the reaction pathways **1–9** shown in Scheme 2 are summarized in Table 1 and presented separately for each of the pathways studied.

3.2.1. Pathway 1. In accordance with the experimentally observed high stability of 1,2-μ **P**, DMRG-CASPT2(26e,20o) calculations exclude its direct attack on the C$_{10}$–H bond, i.e., pathway **1**. This was considered to proceed either via O–O cleavage preceding C$_{10}$–H attack or via a concerted O–O and C$_{10}$–H bond splitting (as mapped by a two-dimensional scan of the potential energy surface).[79] In both cases (both shown in Table 1), the *in vacuo* energy barrier is 90 kJ mol^{-1} or higher, and with steric and electrostatic QM/MM corrections (Table S1), the barrier is higher than ~115 kJ mol^{-1}, significantly above the experimental free energy barrier of desaturation of 62 kJ mol^{-1}, inferred from k_{cat} = 95 s^{-1}.[80] Nevertheless, the product has an energy comparable to the reactant ($\Delta E_{DMRG-CASPT2}$ = −3.9 kJ mol^{-1}; $\Delta E_{DMRG-CASPT2/MM}$ = 11.1 kJ mol^{-1}).

3.2.2. Pathway 2. The 1,1-μ hydroperoxo Fe^{III}Fe^{III} species, the product of an energetically accessible proton-assisted O$_2$ activation pathway (**prot-2** in Scheme 1) was found to be a very promising candidate for C$_{10}$–H bond activation. The DMRG-CASPT2(26e,22o) calculations predict an activation energy of $\Delta E^\ddagger \approx 55$ kJ mol^{-1}, and our estimate[81] of the activation Gibbs free energy (eqs 1 and 2) is $\Delta G^\ddagger \approx 72$–85 kJ mol^{-1} (Figure 3) with kinetic isotope effect of ~3–4 (Table S2). These values are in reasonable agreement with free energy barrier of 62 kJ mol^{-1} derived from the kinetic experiments and with the intrinsic isotope effect of ~10 (ref 80). Moreover, the reaction
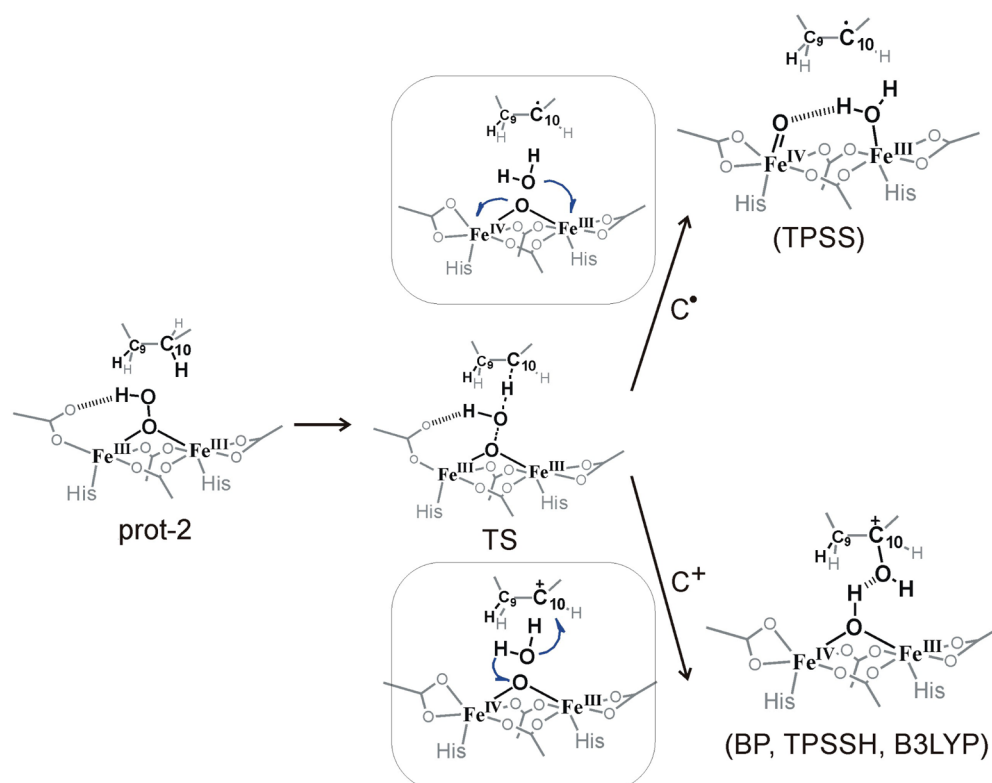
Figure 5. Two possible pathways (hydride vs H atom abstraction) observed in QM/MM optimizations using different DFT functionals (here the example for **prot-2** from Scheme 1 [$\equiv$ **R$_2$** from Scheme 2]). Hydride transfer toward the O$_2$-activated binuclear iron center leads to the formation of C$_{10}^+$ cation instead of C$_{10}^\bullet$ radical, ultimately leading to a hydroxylated product. For analysis of the energetic contributions, *see* Table S4. Similar results (BP86 H$^-$ vs TPSS H$^\bullet$ transfer) were also observed for the water-assisted pathway **3**.

yields the thermodynamically accessible product **P$_2$**, lying 3.4 kJ mol^{-1} above the reactant **R$_2$** (Figure 3). After inclusion of QM/MM corrections from Table S1 and thermal free-energy contributions,[81] the final $\Delta G(\mathbf{R_2} \rightarrow \mathbf{P_2})$ is between -10 and -19 kJ mol^{-1}. In the product, the resultant Fe$_A^{IV}$=O unit in **P$_2$** is in a favorable orientation with respect to the C$_9$–H bond, and the O–H$_{C9}$ distance is 2.88 Å, suggesting the feasibility of a second H atom abstraction from the C$_9$ site as a following step in the catalytic cycle.

Despite significant geometrical changes in going from **R$_2$** to **TS$_2$** (O–O: 1.40 vs 1.71 Å; C$_{10}$–H: 1.11 vs 1.23 Å), the electronic structures of **TS$_2$** and **R$_2$** are very similar. Both are characterized by antiferromagnetically coupled high-spin ($S = 5/2$) Fe^{III}···Fe^{III} centers (total $S = 0$) with the hydroperoxide moiety in 1,1-μ binding mode. The analysis of the DMRG-CASSCF wave function at the transition-state geometry suggests a strong electronic coupling between the O$_A$–H fragment from the hydroperoxo group (Fe$_2$–O$_B$–O$_A$H) and the C$_{10}$–H bond. This is perhaps best illustrated by the difference in composition and occupation of molecular orbitals participating in the formation of the $\{O_B\cdots HO_A\cdots H\cdots C_{10}\}$ arrangement in **TS$_2$** (Figure 4). Namely, in **TS$_2$**, the originally pure O–O σ and σ^* orbitals from **R$_2$** (with orbital occupations close to 2 and 0, respectively) become delocalized over the $\{O\cdots O\cdots H\cdots C\}$ fragment with antibonding interaction with the H–C σ orbital and correlated, which is reflected by their occupations of 1.88 and 0.13, respectively. On the other hand, the occupation of Fe d orbitals remains essentially unchanged (d-orbital occupations vary between 0.96 and 1.04 in **R$_2$** and between 0.94 and 1.06 in **TS$_2$**); the **R$_2$** $\rightarrow$ **TS$_2$** transition is thus

not accompanied by change in the oxidation state of either of the two Fe centers.

Proceeding from **TS$_2$** to **P$_2$** is, according to the DMRG-CASPT2 results, accompanied by the oxidation of Fe$_A$(III) center and results in an [Fe$_A^{IV}$=O···Fe$_B^{III}$–OH$_2$···C$^\bullet$] electronic structure for **P$_2$** (see Figure 4), indicating that the C$_{10}$–H bond has cleaved homolytically. In addition, as can be seen in Figure S3, a reactive Fe$_A^{IV}$=O unit with high-spin ($S = 2$) $\delta^1\pi^{*2}\sigma_1^{*1}$ electronic structure is generated, which implies the feasibility of subsequent C$_9$–H bond cleavage (see, for example refs 30 and 82 and references therein) that would complete the desaturation of the substrate. Interestingly, the Fe$_A^{IV}$=O σ_2 and σ_2^* occupation numbers of 1.69 and 0.31 indicate very strong correlation between these two orbitals and, therefore, partial radical (oxyl) character on the oxo group, whose weight would further increase with elongation of Fe–O bond in approaching the transition state of C$_9$–H bond cleavage. Indeed, a nearly colinear orientation of the C$_9$–H bond relative to the $S = 2$ Fe$_A^{IV}$=O bond axis is present in **P$_2$** ($<$Fe$_A$–O–H$_{C9} \approx 160°$) suggesting that the second H atom abstraction should proceed via a σ mechanism (well-characterized in literature),[30b,82a,83] which is controlled by spin polarization from the oxo p$_z$-based σ_2 to d$_{z^2}$(Fe)-based σ_2^* orbital along the reaction coordinate.

Interestingly, several DFT methods (BP86, B3LYP, TPSSh) predict that this reaction pathway corresponds to hydride instead of H atom abstraction (Figure 5). Upon leaving the TS toward the product in the QM(DFT)/MM geometry optimization, a carbocation on the substrate is formed, while the irons remain in the +3 oxidation state. In the resulting H$_2$O$_A$···C$_{10}^+$ species, substrate hydroxylation (C$_{10}$–O$_A$H)

occurs in a barrierless process, with the concomitant formation of a $Fe_A^{III}-O_BH-Fe_B^{III}$ structure. In contrast, the DMRG results suggest that this alternative possibility of hydride abstraction from the C_{10} site is unlikely. Namely, at the TS_2 geometry, an electronic structure corresponding to hydride transfer is estimated to be much higher in energy than that corresponding to H atom abstraction.[84] These popular DFT functionals thus predict a qualitatively wrong PES, directing the reaction into a "hydroxylation trap" (see also Section 3.3 and Figure 5), which is presumably avoided in reality because the correct activation barrier for the hydride abstraction reaction step is prohibitively high. DMRG and DFT agree that the "trap" is deep, with the "P_2 hydroxylated" structure being thermodynamically highly stable ($\Delta E_{DMRG-CASPT2} = -254.6$ kJ mol^{-1}, Table 1).

3.2.3. Pathway 3. The water-assisted H atom abstraction pathway has a very high DMRG-CASPT2($34e,26o$) activation barrier (150 kJ mol^{-1}) and can be safely ruled out. The barrier is significantly higher than that for the proton-assisted pathway 2 despite the reactive [$Fe^{III}-OOH$] unit attacking the $C_{10}-H$ bond in both pathways (compare TS_2 and TS_3 in Scheme 2). A geometric difference between transition states TS_2 and TS_3 is evident from Figure S4: the first has an early transition state in terms of $O-OH$ bond length along the $C_{10}-H$ attack reaction coordinate (1.71 Å), whereas the latter has a later transition state ($d(O-OH) = 2.05$ Å) with a stronger correlation between the σ and σ^* orbitals in the $\{O\cdots HO\cdots H\cdots C_{10}\}$ unit (occupation numbers are 1.65 and 0.39 for σ and σ^* in TS_3 vs 1.88 and 0.13 for σ and σ^* in TS_2). These geometric and energetic differences are consequences of the different binding mode of the hydroperoxide moiety in the proton- vs water-assisted activation processes. In the proton-assisted pathway 2, the hydroperoxide forms a 1,1-μ bridge between two antiferromagnetically coupled Fe^{III} centers. In the water-assisted pathway 3, the hydroperoxide is bound to only one of the two $S = 5/2$ Fe^{III} sites, which results in lowered electrophilicity and thus reactivity toward an aliphatic C−H bond as compared to pathway 2.

3.2.4. Pathways 4 and 5. The homolytic O−O bond cleavage starting from the carboxy-protonated **prot-1** structure (Scheme 1 and $R_4 \rightarrow TS_4 \rightarrow P_4$ in Scheme 2) was originally found to be barrierless (using the BP86 functional) in the RNR.[15] However, the energetics of this step is dependent on the DFT functional (the barrier varying from 0 to ~170 kJ mol^{-1}).[16] This finding precludes evaluation of the feasibility of this reaction at the DFT level of theory, and its relevance to the activation of the **P** intermediate toward $C_{10}-H$ bond cleavage cannot be inferred. On the other hand, the DMRG-CASPT2-($26e,20o$) calculations clearly show that the activation barrier for pathway 4 is too high (118 kJ mol^{-1}) to compete even with the direct $C_{10}-H$ attack in pathway 1. Thus, the O−O bond cleavage is not a feasible alternative to the direct proton-assisted reaction mechanism for Δ^9D.[85] From a qualitative perspective, the large barrier associated with the O−O bond cleavage in pathway 4 correlates with a large σ/σ^* interaction (DMRG occupation numbers are 1.75 and 0.28 for σ and σ^*, respectively) associated with the late transition state ($d(O-O) = 1.9$ Å; Figure 5).

The same conclusion that the O−O bond cleavage is not a feasible process in Δ^9D also holds true for pathway 5, in which 1,2-μ O_2^{2-} is protonated ($R_5 \rightarrow P_5$ in Scheme 2). Upon elongating the O−O bond, the DMRG energy increases to ~155 kJ mol^{-1}, giving rise to the highly unstable P_5 with the

[$Fe_A^{IV}-OH$ $Fe_B^{IV}=O$] electronic structure (the concerted trajectory, along which the O−O bond splits with concomitant H atom abstraction from C_{10}, was not considered because of the formation of the presumably unstable [$Fe_A^{IV}-OH$ $Fe_B^{III}-OH$] product). Beyond their relevance for Δ^9D, our computational results thus suggest that O−O bond cleavage during the $P \rightarrow X$ conversion in RNR does not occur prior to reduction of the diferric active site.

3.2.5. Pathways 6−9. Although the activation of the peroxy-level intermediate in Δ^9D by an electron was not experimentally supported,[55] it is interesting to note that all reaction pathways investigated in this study with an exogenous electron have relatively small barriers, and the corresponding products lie in most cases much lower in energy than the reactants (Scheme 2). Thus, we include these results for consideration of the reaction mechanism that may be relevant to RNR.

Concerning pathway 6, the addition of an extra electron to the **P** intermediate gives 1,2-μ $O_2^{\bullet-}$ $Fe_A^{II}Fe_B^{II}$ structure (R_6 in Scheme 2 and Table 1), which can readily undergo O−O bond cleavage (with an *in vacuo* DMRG-CASPT2($27e,20o$) barrier of 40 kJ mol^{-1}) to form the [$Fe_A^{IV}=O^{2-}$ $Fe_B^{III}-O^{2-}$] product P_6, isoenergetic with R_6. A $1e^-$ triggered O−O cleavage is even more favorable in the presence of an exogenous proton on the carboxylate (pathway 8), with no DMRG-CASPT2($27e,20o$) barrier, leading to the [$Fe_A^{III}-OH$ $Fe_B^{IV}=O$] product P_8, which is much more stable than R_8 ($\Delta E \sim -64$ kJ mol^{-1}). Importantly, the product P_8 has a reactive high-spin ($S = 2$) $Fe_B^{IV}=O$ unit σ-oriented with respect to the $C_{10}-H$ bond (with $H_{C_{10}}\cdots O_{FeB}$ distance of 2.34 Å), which indicates the feasibility of a subsequent H atom abstraction step. Conversely, P_6 with an $S = 2$ $Fe_A^{IV}=O$ group would initiate desaturation at the C_9 site, which is inconsistent with experimental observations.[12] In contrast to O−O cleavage in the analogous R_4 activated by carboxy protonation, the 1,2-μ O−O moiety in the $1e^-$ activated R_6 has superoxide character that remains along the $R_6 \rightarrow TS_6$ pathway ($d(O-O) = 1.75$ Å). Owing to the larger O−O force constant of superoxide relative to that of peroxide, TS_6 (with 1,2-μ $O_2^{\bullet-}$ character) is formed earlier along the O−O elongation pathway than TS_4 (with 1,2-μ O_2^{2-} character); $d(O-O) = 1.75$ and 1.9 Å for TS_6 and TS_4, respectively. This correlates with a lower activation energy for pathway 6 as compared to pathway 4. Interestingly, in R_8 where both the extra electron and the extra proton on the Glu residue terminally bound to the Fe_A center are present, peroxide character is induced in the 1,2-μ O_2 bridge (see the electronic structure of R_8 in Table 1). This triggers the spontaneous homolytic cleavage of the O−O bond. Among the reactions investigated in this study, the (H^+,e^-)-activated $R_8 \rightarrow P_8$ pathway seems most relevant for the conversion of the **P** to the **X** intermediate in RNR.

Pathways 7 and 9 are $1e^-$ reduced analogs of pathways 2 and 3. On pathway 7, as shown in Table 1, the effect of reducing the (5C,6C) 1,1-μ hydroperoxy $Fe^{III}Fe^{III}$ species to its $Fe^{II}Fe^{III}$ counterpart on the reaction barrier for H atom abstraction from the C_{10} site is small ($\Delta E^{\ddagger}_{in-vacuo} = 65$ kJ mol^{-1}), while the stabilization of P_7 relative to R_7 is much larger as compared to P_2 relative to R_2 in pathway 2. On the other hand, $1e^-$ reduction of R_3 to R_9 has a considerable effect on the *in vacuo* DMRG activation barrier (lowering it from 150 to 87 kJ mol^{-1}) and reaction energy (from 9 to −68 kJ mol^{-1}). Thus, the computed barriers for pathways 7 and 9 are low but non-negligible, suggesting that in the presence of an exogenous

Table 2. Activation and Reaction (in italics) Energies (in kJ mol⁻¹) for the Nine Studied Reaction Pathways (Scheme 2)^a

reaction	1	2^c	3^c	4	5	6	7	8	9	MAD^d	MaxD^e
DMRG-CASPT2	29	55	150	25	42	40	65	−6	87	–	–
	−65	*3*	*9*	*−19*	*155*	*0*	*−79*	*−64*	*−68*		
	>90^b			118^b							
	−4^b			*14^b*							
BP86	134	56	74	4	25	21	46	3	51	22	−76
	39	*−61*	*−27*	*−27*	*−83*	*−27*	*−92*	*−72*	*−65*	*43*	*−238*
TPSS	144	64	138	−1	22	25	52	7	63	13	−24
	44	*−50*	*−24*	*−23*	*−73*	*−18*	*−76*	*−60*	*−54*	*39*	*−228*
TPSSh	140	81	177	60	83	65	66	20	82	19	+41
	63	*−15*	*25*	*45*	*15*	*52*	*−55*	*−36*	*−41*	*34*	*−140*
B3LYP	132	90^f	213	117	138	97	74	36	115	41	+96
	76	*8*	*59*	*103*	*91*	*98*	*−51*	*−22*	*−8*	*39*	*+98*
B3LYP-D3	123	92	212	109	126	93	77	36	118	40	+84
	67	*−3*	*58*	*98*	*82*	*95*	*−63*	*−18*	*−14*	*38*	*+95*
M06	157	119	229	147	98	−2	48	45	58	42	+79
	107	*34*	*80*	*171*	*153*	*13*	*−143*	*102*	*−117*	*44*	*+166*
τ-HCTH	142	68	171	97	105	−43	39	24	62	33	−83
	64	*−33*	*25*	*46*	*−2*	*−80*	*−123*	*−16*	*−98*	*46*	*−157*
M06-L	161	88	183	122	95	−56	55	29	48	37	−96
	77	*−14*	*36*	*75*	*37*	*−80*	*−*	*8*	*−108*	*43*	*−118*
ωB97X-D	124	126	239	141	151	62	46	49	150	54	+109
	92	*33*	*79*	*150*	*149*	*69*	*−98*	*79*	*−22*	*43*	*+143*

^{a}The corresponding DFT spin densities on the key atoms are shown in Table S3. The presented values represent *in vacuo* single-point energies of the QM regions at the QM(BP86/def2-SVP)/MM equilibrium geometries. The steric, ΔE_{MM23}, and electrostatic ΔE_{ptchgs} (eq 1) QM/MM corrections to *in vacuo* activation and reaction energies are listed in Table S1. ^{b}Calculated as the difference between maxima and minima of the DMRG-CASPT2 energy along the one-dimensional reaction path calculated at the QM(BP86/def2-SVP)/MM level. Note that the location of these extrema are shifted along the reaction coordinate with respect to those of the QM(BP86/def2-SVP)/MM PES (for an example, see Figure S5). ^{c}In order to prevent the formation of the hydroxylated substrate due to H⁻ instead of H• transfer on the O₂-activated diferric center, the product structure was obtained first using QM(TPSS/def2-SVP)/MM with subsequent geometry reoptimization at the QM(BP86/def2-SVP)/MM level. See Figure 5 and Table S4 for more details ^{d}MAD $= 1/n \sum_{i=1}^{n} |\Delta E_{DFT}^{(‡)} - E_{DMRG-CASPT2}^{(‡)}|$; For evaluation of MADs for all DFT functionals, pathways **1** and **4** were not considered. ^{e}MaxD is the maximum value from the set of elements $\{\Delta E_{DFT}^{(‡)} - E_{DMRG-CASPT2}^{(‡)}\}_{i=1}^{n}$ (maximum deviation); For evaluation of MaxDs for all DFT functionals, pathways **1** and **4** were not considered. ^{f}The DFT calculations with scalar relativistic corrections (through second-order Douglas−Kroll−Hess [DKH2] treatment combined with the DKH-TZV basis set as implemented in the ORCA 2.9 program)[57,87,88] differ only by few kJ mol⁻¹ from nonrelativistic DFT results (e.g., $\Delta E_{B3LYP}^{(‡)}$ vs $\Delta E_{DKH2-B3LYP}^{(‡)}$: 90 vs 88 kJ mol⁻¹ for the reaction pathway **2**).

electron as in RNR, the barrier-free pathway **8** involving O−O cleavage is likely the most relevant.

3.3. Comparison of Popular DFT Functionals for Reactivity of Binuclear Nonheme Iron Systems using DMRG-CASPT2 as the Reference. In the preceding sections, we employed the DMRG-CASPT2-calculated reaction and activation energies to distinguish among various mechanistic possibilities. Confidence to do so was gained from the fact that DMRG-CASSCF offers a physically correct description of the wave function in these highly multireference systems, and together with the perturbative treatment of dynamic correlation, a reasonable accuracy and qualitatively correct picture can be expected ("right answer for the right reason"). Nevertheless, there are several potential caveats of the DMRG methodology used in this study (e.g., basis set effects, usage of equilibrium QM(DFT)/MM geometries that may not coincide with the maxima/minima along the DMRG-CASPT2 reaction coordinate, size of the active space, double-shell *d* effect), which are discussed in more detail in the Supporting Information.

Despite these issues, we use the unique set of DMRG-CASPT2 data obtained for our model systems described in the previous section to compare the performance of some popular DFT functionals, which are generally the method of choice in QM and QM/MM studies of (metallo)enzymatic reactivity. To this goal, we calculated the energies of reactants, transition states, and products for all nine reaction pathways depicted in Scheme 2. The results are summarized in Table 2.

In accordance with past results,[86] the pure generalized gradient approximation (GGA) functionals, such as BP86, and the pure meta-GGAs, such as TPSS, were found to overstabilize transition states and products as compared to reactants. In addition, both functionals incorrectly predict the proton-assisted O−O bond cleavage (pathways **4** and **5**) to be energetically more favorable than C_{10}−H bond cleavage through (5C,6C) 1,1-μ HOO−Fe^{III}Fe^{III} (pathway **2**) and thus completely alter the mechanistic description of the Δ⁹D catalysis. This discrepancy is most pronounced for pathway **5** (i.e., cleavage of the 1,2-μ HOO⁻ bridge), where the DFT product is significantly more stable than the DFT reactant, while the opposite is the case at the DMRG-CASPT2 level of theory. Interestingly, this cannot be attributed to the difference in electronic configuration obtained for the ground state of the P_5 product, because both DMRG-CASPT2 and DFT (BP86 and TPSS, see Table S3 for results of Mulliken spin-population analysis) predict the [Fe^{IV}(OH) Fe^{IV}=O] formal oxidation states. Despite these shortcomings, the mean absolute deviation (MAD) between the BP86 or TPSS values and the reference (DMRG) is reasonably small for activation barriers (MAD of 22 and 13 kJ mol⁻¹, respectively), while it is considerably larger for reaction energies (MAD of 43 and 39 kJ mol⁻¹) as shown in the last column of Table 2.

Scheme 3. Suggested Proton-Assisted Mechanism of O_2 Activation and Substrate $C_{10}-H$ Bond Cleavage Leading to Desaturation in the Catalytic Cycle of Δ^9D^a
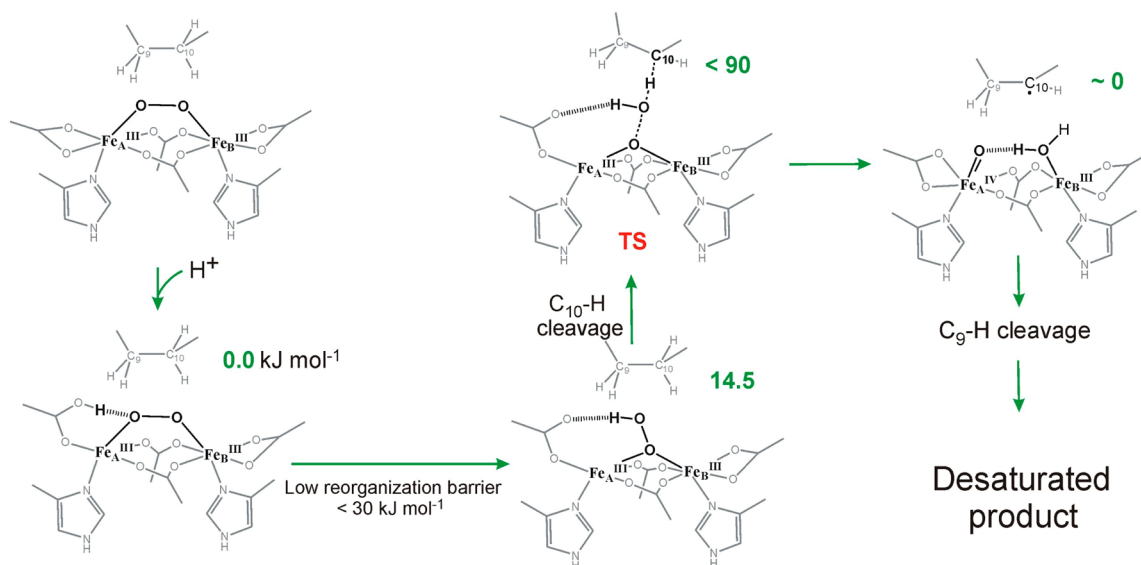
^{a}Relative Gibbs free energies (in kJ mol^{-1}) are estimated according to eq 2.

Two other popular meta-GGA functionals, M06-L and τ-HCTH, predict in general significantly higher barriers, whose MAD values are larger than those obtained from BP86 and TPSS methods (37 and 33 kJ mol^{-1}, respectively), with the most diverging results obtained for pathway 6 (Table 2). For this pathway, it is noteworthy that the M06-L and τ-HCTH values also differ enormously from the results of other DFT methods, although the spin populations remain similar (Table S3).

On average, most tested hybrid functionals (B3LYP, M06, and ωB97X-D) yield results of (in)accuracy similar to meta-GGAs, with MAD $\approx$ 30−50 kJ mol^{-1}. The only exception is the hybrid TPSSh functional (with 10% of Hartree−Fock exchange), which is found to be the most consistent with the DMRG-CASPT2 results, having MADs of 19 and 34 kJ mol^{-1} for activation and reaction energies, respectively.

The inclusion of empirical dispersion corrections does not lead to significant changes in the calculated reaction and activation energies (0−12 kJ mol^{-1}, cf. B3LYP vs B3LYP-D3 results in Table 2); the same holds true for the inclusion of scalar relativistic effects (tested for pathway 2 at the B3LYP level; see Table 2).

Concerning the qualitative picture, as mentioned earlier in the discussion of pathway 2, several DFT functionals erroneously predict hydride instead of H atom abstraction and, therefore, substrate hydroxylation instead of desaturation. As depicted in Figure 5 and quantitatively evaluated in Table S4, only the TPSS functional predicts preference for the hydrogen abstraction pathway (leading to desaturation) over the hydride abstraction (leading to hydroxylation) on the favored pathway 2, and therefore, we cautiously recommend it to be used in the QM and/or QM/MM geometry optimizations of the NHFe$_2$ systems. After locating the qualitatively correct QM(TPSS) or QM(TPSS)/MM stationary points, the TPSSh functional might be used to further improve the accuracy of the energy profiles. In addition, it is also worth stressing that several DFT functionals tend to significantly underestimate peroxide bond length in the Fe^{III}(O−O)$^{2-}$Fe^{III}

complex involved in pathways 1 and 4. As a consequence, highly correlated methods provide an incorrect electronic structure description of the ground state (Fe^{II}(O−O)$^{\bullet-}$Fe^{III}) causing flawed estimates of activation and reaction energies for DFT-optimized geometric structures. Thus, without exploring the DMRG-CASPT2 energy profile along a DFT reaction coordinate, pathways 1 and 4 would be erroneously favored over pathway 2 (see Table 2).

4. CONCLUSIONS

In this study, a full account is given of a reaction coordinate of the nonheme diiron enzyme (Δ^9D) using multireference (quantum entangled) density matrix renormalization group (DMRG) calculations. To the best of our knowledge, this is the first application of this method in modeling a reaction mechanism of a bioinorganic system. Density functional theory is usually considered as the practical method of choice for the NHFe$_2$ systems. However, as can be seen in Table 2, the spread of activation and reaction energies calculated by DFT methods precludes their usage in obtaining (semi)quantitatively or sometimes even qualitatively correct mechanistic and energetic insight into the reaction mechanism. We do not claim that the DMRG-CASPT2 values presented can be regarded as "gold standard" as, for example, large basis set CCSD(T) calculations of smaller closed-shell systems. Still, the DMRG-CASPT2 method, allowing for a physically sound description of these highly multireference systems, can be expected to provide "right answers for the right reason" in distinguishing between qualitatively different and competing reaction pathways. This approach thus adds a significant value to the computational studies of the NHFe$_2$ systems. The present DMRG-CASPT2 study allowed the formulation of a plausible mechanism of the desaturation reaction catalyzed by the Δ^9D, graphically depicted in Scheme 3. Key steps include proton activation of the **P** intermediate, reorganization to 1,1-μ hydroperoxo Fe^{III}Fe^{III} structure, H atom abstraction from C_{10} by the hydroperoxo unit in concert with O−O bond cleavage, and H atom abstraction from C_9 by the resulting Fe^{IV}O moiety.

Further studies on the Δ^9D reaction mechanism including the factors responsible for preferring desaturation over hydroxylation as well as development and further applications of the DMRG methods in bioinorganic chemistry are ongoing in our laboratories.

■ ASSOCIATED CONTENT

Ⓢ Supporting Information

Figures S1–S5, Tables S1–S6, the equilibrium geometries of QM regions of all systems studied here, and the structure of the full solvated protein obtained from the QM/MM calculations (in PDB format). This material is available free of charge via the Internet at http://pubs.acs.org.

■ AUTHOR INFORMATION

Corresponding Authors
solomone@stanford.edu
rulisek@uochb.cas.cz
srnec@jh-inst.cas.cz

Notes
The authors declare no competing financial interest.

■ ACKNOWLEDGMENTS

■ REFERENCES

(1) Fontecave, M.; Ménage, S.; Duboc-Toia, C. Coord. Chem. Rev. 1998, 178, 1555–1572.
(2) Solomon, E. I.; Brunold, T. C.; Davis, M. I.; Kemsley, J. N.; Lee, S. K.; Lehnert, N.; Neese, F.; Skulan, A. J.; Yang, Y. S.; Zhou, J. Chem. Rev. 2000, 100, 235–349.
(3) Lee, D.; Pierce, B.; Krebs, C.; Hendrich, M. P.; Huynh, B. H.; Lippard, S. J. J. Am. Chem. Soc. 2002, 124, 3993–4007.
(4) Koehntop, K. D.; Emerson, J. P.; Que, L. J. Biol. Inorg. Chem. 2005, 10, 87–93.
(5) Cranswick, M. A.; Meier, K. K.; Shan, X. P.; Stubna, A.; Kaizer, J.; Mehn, M. P.; Munck, E.; Que, L. Inorg. Chem. 2012, 51, 10417–10426.
(6) Makris, T. M.; Chakrabarti, M.; Münck, E.; Lipscomb, J. D. Proc. Natl. Acad. Sci. U.S.A. 2010, 107, 15391–15396.
(7) (a) Wong, S. D.; Srnec, M.; Matthews, M. L.; Liu, L. V.; Kwak, Y.; Park, K.; Bell, C. B., III; Alp, E. E.; Zhao, J.; Yoda, Y.; Kitao, S.; Seto, M.; Krebs, C.; Bollinger, J. M.; Solomon, E. I. Nature 2013, 499, 320–323. (b) Solomon, E. I.; Light, K. M.; Liu, L. V.; Srnec, M.; Wong, S. D. Acc. Chem. Res. 2013, 46, 2725–2739. (c) Vaillancourt, F. H.; Yeh, E.; Vosburg, D. A.; Garneau-Tsodikova, S.; Walsh, C. T. Chem. Rev. 2006, 106, 3364–3378.
(8) (a) Wallar, B. J.; Lipscomb, J. D. Chem. Rev. 1996, 96, 2625–2657. (b) Tinberg, C. E.; Lippard, S. J. Acc. Chem. Res. 2011, 44, 280–288.
(9) (a) Nordlund, P.; Reichard, P. Annu. Rev. Biochem. 2006, 75, 681–706. (b) Minnihan, E. C.; Nocera, D. G.; Stubbe, J. Acc. Chem. Res. 2013, 46, 2524–2535.
(10) Pikus, J. D.; Studts, J. M.; Achim, C.; Kauffmann, K. E.; Münck, E.; Steffan, R. J.; McClay, K.; Fox, B. G. Biochemistry 1996, 35, 9106–9119.
(11) Tinberg, C. E.; Lippard, S. J. Acc. Chem. Res. 2011, 44, 280–288.
(12) Fox, B. G.; Lyle, K. S.; Rogge, C. E. Acc. Chem. Res. 2004, 37, 421–429.
(13) Lindqvist, Y. In Handbook of Metalloproteins; Messerschmidt, A., Huber, R., Wieghardt, K., Poulos, T., Eds.; Wiley: New York, 2001; pp 725–737.
(14) Bochevarov, A. D.; Li, J. N.; Song, W. J.; Friesner, R. A.; Lippard, S. J. J. Am. Chem. Soc. 2011, 133, 7384–7397.
(15) Jensen, K. P.; Bell, C. B.; Clay, M. D.; Solomon, E. I. J. Am. Chem. Soc. 2009, 131, 12155–12171.
(16) Srnec, M.; Rokob, T. A.; Schwartz, J. K.; Kwak, Y.; Rulíšek, L.; Solomon, E. I. Inorg. Chem. 2012, 51, 2806–2820.
(17) Song, W. J.; Lippard, S. J. Biochemistry 2011, 50, 5391–5399.
(18) Shu, L.; Nesheim, J. C.; Kauffmann, K.; Münck, E.; Lipscomb, J. D.; Que, L. Science 1997, 275, 515–518.
(19) Bollinger, J. M.; Stubbe, J.; Huynh, B. H.; Edmondson, D. E. J. Am. Chem. Soc. 1991, 113, 6289–6291.
(20) Sturgeon, B. E.; Burdi, D.; Chen, S. X.; Huynh, B. H.; Edmondson, D. E.; Stubbe, J.; Hoffman, B. M. J. Am. Chem. Soc. 1996, 118, 7551–7557.
(21) Han, W.-G.; Noodleman, L. Inorg. Chem. 2008, 47, 2975–2986.
(22) Bochevarov, A. D.; Friesner, R. A.; Lippard, S. J. J. Chem. Theory Comput. 2010, 6, 3735–3749.
(23) Siegbahn, P. Inorg. Chem. 1999, 38, 2880–2889.
(24) (a) Han, W. G.; Noodleman, L. Dalton Trans. 2009, 30, 6045–6057. (b) Han, W. G.; Noodleman, L. Inorg. Chem. 2011, 50, 2302–2320.
(25) Rogge, C. E.; Fox, B. G. Biochemistry 2002, 41, 10141–10148.
(26) Guy, J. D.; Whittle, E.; Moche, M.; Lengqqvist, J.; Lindqvist, Y.; Shanklin, J. Proc. Natl. Acad. Sci. U. S. A. 2011, 108, 16594–16599.
(27) Behrouzian, B.; Savile, C. K.; Dawson, B.; Buist, P. H.; Shanklin, J. J. Am. Chem. Soc. 2002, 124, 3277–3283.
(28) Cooper, H. L. R.; Mishra, G.; Huang, X.; Pender-Cudlip, M.; Austin, R. N.; Shanklin, J.; Groves, J. T. J. Am. Chem. Soc. 2012, 134, 20365–20375.
(29) Vancoillie, S.; Zhao, H.; Tran, V. T.; Hendrickx, M. F. A.; Pierloot, K. J. Chem. Theory Comput. 2011, 7, 3961–3977.
(30) (a) Srnec, M.; Wong, S. D.; England, J.; Que, L., Jr.; Solomon, E. I. Proc. Natl. Acad. Sci. U.S.A. 2012, 109, 14326–14331. (b) Neidig, M. L.; Decker, A.; Choroba, O. W.; Huang, F.; Kavana, M.; Moran, G. R.; Spencer, J. B.; Solomon, E. I. Proc. Natl. Acad. Sci. U.S.A. 2006, 103, 12966–12973.
(31) Delcey, M. G.; Pierloot, K.; Phung, Q. M.; Vancoillie, S.; Lindh, R.; Ryde, U. Phys. Chem. Chem. Phys. 2014, 16, 7927–7938.
(32) (a) Chen, H.; Ikeda-Saito, M.; Shaik, S. J. Am. Chem. Soc. 2008, 130, 14778–14790. (b) Chen, H.; Song, J.; Lai, W.; Wu, W.; Shaik, S. J. Chem. Theory Comput. 2010, 6, 940–953. (c) Chen, H.; Lai, W.; Shaik, S. J. Phys. Chem. B 2011, 115, 1727–1742.
(33) Chalupský, J.; Neese, F.; Solomon, E. I.; Ryde, U.; Rulíšek, L. Inorg. Chem. 2006, 45, 11051–11059.
(34) Vancoillie, S.; Chalupský, J.; Ryde, U.; Solomon, E. I.; Pierloot, K.; Neese, F.; Rulíšek, L. J. Phys. Chem. B 2010, 114, 7692–7702.
(35) Rulíšek, L.; Ryde, U. Coord. Chem. Rev. 2013, 257, 445–458.
(36) Friedle, S.; Reisner, E.; Lippard, S. J. Chem. Soc. Rev. 2010, 39, 2768–2779.
(37) Riley, K. E.; Pitoňák, M.; Jurečka, P.; Hobza, P. Chem. Rev. 2010, 110, 5023–5063.
(38) (a) White, S. R. Phys. Rev. Lett. 1992, 69, 2863–2866. (b) White, S. R. Phys. Rev. B 1993, 48, 10345–10356.

15989

dx.doi.org/10.1021/ja506934k | J. Am. Chem. Soc. 2014, 136, 15977–15991

(39) Legeza, Ö.; Noack, R.; Sólyom, J.; Tincani, L. In *Computational Many-Particle Physics, Lecture Notes in Physics*; Fehske, H., Schneider, R., Weibe, A., Eds.; Springer: Berlin, 2008; Vol. *739*, pp 653−664.

(40) Marti, K. H.; Reiher, M. *Z. Phys. Chem.* **2010**, *224*, 583−599.

(41) Chan, G. K.-L.; Sharma, S. *Annu. Rev. Phys. Chem.* **2011**, *62*, 465−481.

(42) Kurashige, Y. *Mol. Phys.* **2014**, *112*, 1485−1494.

(43) Ghosh, D.; Hachmann, J.; Yanai, T.; Chan, G. K.-L. *J. Chem. Phys.* **2008**, *128*, 144117.

(44) (a) Yanai, T.; Chan, G. K.-L. *J. Chem. Phys.* **2006**, *124*, 194106. (b) Yanai, T.; Chan, G. K.-L. *J. Chem. Phys.* **2007**, *127*, 104107. (c) Neuscamman, E.; Yanai, T.; Chan, G. K.-L. *J. Chem. Phys.* **2009**, *130*, 124102.

(45) (a) Kurashige, Y.; Yanai, T. *J. Chem. Phys.* **2011**, *135*, 094104. (b) Kurashige, Y. *Mol. Phys.* **2014**, *112*, 1485−1494.

(46) Yanai, T.; Kurashige, Y.; Neuscamman, E.; Chan, G. K.-L. *J. Chem. Phys.* **2010**, *132*, 024105.

(47) Cramer, C. J.; Włoch, M.; Piecuch, P.; Puzzarini, C.; Gagliardi, L. *J. Phys. Chem. A* **2006**, *110*, 1991−2004.

(48) Marti, K. H.; Ondik, I. M.; Moritz, G.; Reiher, M. *J. Chem. Phys.* **2008**, *128*, 014104.

(49) Barcza, G.; Legeza, Ö.; Marti, K. H.; Reiher, M. *Phys. Rev. A* **2011**, *83*, 012508.

(50) Kurashige, Y.; Yanai, T. *J. Chem. Phys.* **2009**, *130*, 234114.

(51) Barcza, G.; Legeza, Ö; Marti, K. H.; Reiher, M. *Phys. Rev. A* **2011**, *83*, 012508.

(52) Kurashige, Y.; Chan, G. K.-L.; Yanai, T. *Nat. Chem.* **2013**, *5*, 660−666.

(53) Saleh, L.; Krebs, C.; Ley, B. A.; Naik, S.; Huynh, B. H.; Bollinger, J. M., Jr. *Biochemistry* **2004**, *43*, 5953−5964.

(54) Murray, L. J.; Naik, S. G.; Ortillo, D. O.; Garcia-Serres, R.; Lee, J. K.; Huynh, B. H.; Lippard, S. J. *J. Am. Chem. Soc.* **2007**, *129*, 14500−14510.

(55) Fox, B. *private communication*.

(56) (a) Roos, B. O.; Lindh, R.; Malmqvist, P.-Å.; Veryazov, V.; Widmark, P.-O. *J. Phys. Chem. A* **2005**, *109*, 6575−6579. (b) Widmark, P.-O.; Malmqvist, P.-Å.; Roos, B. O. *Theor. Chim. Acta* **1990**, *77*, 291−306.

(57) (a) Douglas, M.; Kroll, N. M. *Ann. Phys. (N.Y.)* **1974**, *82*, 89−155. (b) Hess, B. A. *Phys. Rev. A* **1986**, *33*, 3742−3748. (c) Jansen, G.; Hess, B. A. *Phys. Rev. A* **1989**, *39*, 6016−6017.

(58) In a standard DMRG terminology, the DMRG-CASSCF active orbitals are regarded as sites of a one-dimensional lattice, along which we move forward and backward during the sweep algorithm until the desired convergence is achieved. Since the correlation is treated most accurately between sites lying spatially close to each other, the accuracy of DMRG-CASSCF results critically depends on the order of the active orbitals (as well as on the number of renormalized many-electron basis functions). As a general rule, the ordering of localized active orbitals should follow as closely as possible the bonding situation in studied molecules.

(59) Pipek, J.; Mezey, P. G. *J. Chem. Phys.* **1989**, *90*, 4916−4926.

(60) Zgid, D.; Nooijen, M. *J. Chem. Phys.* **2008**, *128*, 014107.

(61) Ahlrichs, R.; Bär, M.; Häser, M.; Horn, H.; Kölmel, C. *Chem. Phys. Lett.* **1989**, *162*, 165.

(62) Frisch, M. J.; Trucks, G. W.; Schlegel, H. B.; Scuseria, G. E.; Robb, M. A.; Cheeseman, J. R.; Scalmani, G.; Barone, V.; Mennucci, B.; Petersson, G. A.; Nakatsuji, H.; Caricato, M.; Li, X.; Hratchian, H. P.; Izmaylov, A. F.; Bloino, J.; Zheng, G.; Sonnenberg, J. L.; Hada, M.; Ehara, M.; Toyota, K.; Fukuda, R.; Hasegawa, J.; Ishida, M.; Nakajima, T.; Honda, Y.; Kitao, O.; Nakai, H.; Vreven, T.; Montgomery, J. A., Jr.; Peralta, J. E.; Ogliaro, F.; Bearpark, M.; Heyd, J. J.; Brothers, E.; Kudin, K. N.; Staroverov, V. N.; Kobayashi, R.; Normand, J.; Raghavachari, K.; Rendell, A.; Burant, J. C.; Iyengar, S. S.; Tomasi, J.; Cossi, M.; Rega, N.; Millam, M. J.; Klene, M.; Knox, J. E.; Cross, J. B.; Bakken, V.; Adamo, C.; Jaramillo, J.; Gomperts, R.; Stratmann, R. E.; Yazyev, O.; Austin, A. J.; Cammi, R.; Pomelli, C.; Ochterski, J. W.; Martin, R. L.; Morokuma, K.; Zakrzewski, V. G.; Voth, G. A.; Salvador, P.; Dannenberg, J. J.; Dapprich, S.; Daniels, A. D.; Farkas, Ö.;

Foresman, J. B.; Ortiz, J. V.; Cioslowski, J.; Fox, D. J. *Gaussian 09*, Revision A.01; Gaussian, Inc.: Wallingford, CT, 2009.

(63) (a) Perdew, J. P. *Phys. Rev. B* **1986**, *33*, 8822−8824. (b) Becke, A. D. *Phys. Rev. A* **1988**, *38*, 3098−3100.

(64) Zhao, Y.; Truhlar, D. G. *J. Chem. Phys.* **2006**, *125*, 194101.

(65) Tao, J.; Perdew, J. P.; Staroverov, V. N.; Scuseria, G. E. *Phys. Rev. Lett.* **2003**, *91*, 146401.

(66) Boese, A. D.; Handy, N. C. *J. Chem. Phys.* **2002**, *116*, 9559−9569.

(67) Staroverov, V. N.; Scuseria, G. E.; Tao, J.; Perdew, J. P. *J. Chem. Phys.* **2003**, *119*, 12129−12137.

(68) Becke, A. D. *J. Chem. Phys.* **1993**, *98*, 5648−5652.

(69) Grimme, S.; Antony, J.; Ehrlich, S.; Krieg, H. *J. Chem. Phys.* **2010**, *132*, 154104.

(70) Zhao, Y.; Truhlar, D. G. *Theor. Chem. Acc.* **2008**, *120*, 215−241.

(71) Chai, J.-D.; Head-Gordon, M. *Phys. Chem. Chem. Phys.* **2008**, *10*, 6615.

(72) Eichkorn, K.; Treutler, O.; Öhm, H.; Häser, M.; Ahlrichs, R. *Chem. Phys. Lett.* **1995**, *240*, 283−290.

(73) Eichkorn, K.; Weigen, F.; Treutler, O.; Ahlrichs, R. *Theor. Chim. Acta* **1997**, *97*, 119−124.

(74) (a) Ryde, U. *J. Comput.-Aided Mol. Design* **1996**, *10*, 153−164. (b) Ryde, U.; Olsson, M. H. M. *Int. J. Quantum Chem.* **2001**, *81*, 335−347.

(75) (a) Cornell, W. D.; Cieplak, P.; Bayly, C. I.; Gould, I. R.; Merz, K. M.; Ferguson, D. M.; Spellmeyer, D. C.; Fox, T.; Caldwell, J. W.; Kolman, P. A. *J. Am. Chem. Soc.* **1995**, *117*, 5179−5197.

(76) Skulan, A. J.; Brunold, T. C.; Baldwin, J.; Saleh, L.; Bollinger, J. M., Jr.; Solomon, E. I. *J. Am. Chem. Soc.* **2004**, *126*, 8842−8855.

(77) Broadwater, J. A.; Ai, J.; Loehr, T. M.; Sanders-Loehr, J.; Fox, B. G. *Biochemistry* **1998**, *37*, 14664−14671.

(78) (a) Bollinger, J. M., Jr.; Edmondson, D. E.; Huynh, B. H.; Filley, J.; Norton, J. R.; Stubbe, J. *Science* **1991**, *253*, 292−298. (b) Bollinger, J. M., Jr.; Tong, W. H.; Ravi, N.; Huynh, B. H.; Edmondson, D. E.; Stubbe, J. *J. Am. Chem. Soc.* **1994**, *116*, 8015−8023. (c) Baldwin, J.; Krebs, C.; Ley, B. A.; Edmondson, D. E.; Huynh, B. H.; Bollinger, J. M., Jr. *J. Am. Chem. Soc.* **2000**, *122*, 12195−12206.

(79) The O−O bond length in the R_1 and TS_1 QM(BP86)/MM structures are shorter than 1.40 Å. As a consequence, single-point DMRG-based calculations predict these structures to have a superoxide character, which is inconsistent with the experimentally characterized electronic structure of the intermediate **P**. To remedy this, the two-dimensional scan of the DMRG//QM(BP86)/MM potential energy surface along the $O_A−O_B$ and $O_B···HC_{10}$ coordinates was performed, which gives the peroxo-$Fe^{III}Fe^{III}$ character to both the reactant and the "stepwise" transition state (with the O−O bond 1.55 and 1.80 Å, respectively).

(80) Lyle, K. S.; Haas, J. A.; Fox, B. G. *Biochemistry* **2003**, *42*, 5857−5866.

(81) $\Delta G^{(\ddagger)}$ was estimated using the QM(BP86)/MM corrections taken from Table S1 and thermal free-energy contributions calculated using various functionals. These latter values for the $R_2 \rightarrow TS_2$ ($R_2 \rightarrow P_2$) are −5.6 (−8.7), −18.0 (−16.0), −15.0 (−9.4) and −9.3 (−7.1) kJ mol^{-1} at the X/def2-SVP, X = BP86, TPSS, TPSSh and B3LYP levels of theory, respectively (see Table S2).

(82) (a) Hirao, H.; Que, L., Jr.; Nam, W.; Shaik, S. *Chem.—Eur. J.* **2008**, *14*, 1740−1756. (b) Shaik, S.; Chen, H.; Janardanan, D. *Nat. Chem.* **2011**, *3*, 19−27.

(83) (a) Solomon, E. I.; Wong, S. D.; Liu, L. V.; Decker, A.; Chow, M. S. *Curr. Opin. Chem. Biol.* **2009**, *13*, 99−113. (b) Ye, S.; Neese, F. *Proc. Natl. Acad. Sci. USA* **2011**, *108*, 1228−1233.

(84) The CAS-CI calculation (20 states with orbitals optimized for the ground state) was employed on top of the QM(TPSS)/MM transition-state geometry to identify a charge-transfer excited state with a C_{10}^+—H^- character. Note that such an excited state was not identified among these 20 lowest electronic states, implying a very high barrier for heterolytic cleavage. The high activation energy is very likely overestimated because *in vacuo* calculations do not account for large portion of dynamic electron correlation (only CASSCF level)

and solvation effects stabilizing this charge separation. Additionally, the real transition-state geometry for heterolytic cleavage may differ from the QM(TPSS)/MM transition state, which would further stabilize hydride transfer. However, due to very large energy gap between homolytic and heterolytic C_{10}—H bond cleavage at the present level of theory, it is reasonable to expect that H atom abstraction, after improvement of dynamic electron correlations and inclusion of all solvation and structural factors, remain energetically more favorable.

(85) Such a high barrier thus precludes the formation of the $[Fe_A{}^{IV}=O\ Fe_B{}^{IV}=O]$ intermediate, $\mathbf{P_4}$, which could have otherwise been an important key intermediate in the mechanism. Indeed, it has comparable energy with the reactant $\mathbf{R_4}$ (14.3 kJ mol^{-1}; Table 1), and it can perform H atom abstraction from the C_{10} site through a σ channel ($\Delta E^{\ddagger}_{\text{DMRG-CASPT2}} \approx 60$ kJ mol^{-1}), leading to the $[Fe_A{}^{IV}=O\ Fe_B{}^{III}-OH]$ intermediate (~46 kJ mol^{-1} above $\mathbf{R_4}$), capable of attacking the second C—H bond via its reactive ferryl unit.

(86) Zhao, Y.; Gonzalez-Garcia, N.; Truhlar, D. G. *J. Phys. Chem. A* **2005**, *109*, 2012−2018.

(87) Pantazis, D. A.; Chen, X. Y.; Landis, C. R.; Neese, F. *J. Chem. Theory Comput.* **2008**, *4*, 908−919.

(88) Neese, F. *Wiley Interdiscip. Rev.: Comput. Mol. Sci.* **2012**, *2*, 73−78.